5-2005

Monte Carlo Simulation of Scatter in a Cone-beam X-ray Micro-CT Scanner

Noel F. Black

University of Tennessee - Knoxville

Recommended Citation

Black, Noel F., "Monte Carlo Simulation of Scatter in a Cone-beam X-ray Micro-CT Scanner. " Master's Thesis, University of Tennessee, 2005.
https://trace.tennessee.edu/utk_gradthes/1992

To the Graduate Council:

I am submitting herewith a thesis written by Noel F. Black entitled "Monte Carlo Simulation of Scatter in a Cone-beam X-ray Micro-CT Scanner." I have examined the final electronic copy of this thesis for form and content and recommend that it be accepted in partial fulfillment of the requirements for the degree of Master of Science, with a major in Computer Science.

Jens Gregor, Major Professor

We have read this thesis and recommend its acceptance:

Mike Thomason, Michael Berry

Accepted for the Council:
Carolyn R. Hodges

Vice Provost and Dean of the Graduate School

(Original signatures are on file with official student records.)

To the Graduate Council:

I am submitting herewith a thesis written by Noel F. Black entitled "Monte Carlo Simulation of Scatter in a Cone-beam X-ray Micro-CT Scanner". I have examined the final electronic copy of this thesis for form and content and recommend that it be accepted in partial fulfillment of the requirements for the degree of Master of Science, with a major in Computer Science.

Jens Gregor
Major Professor

We have read this thesis
and recommend its acceptance:

Mike Thomason

Michael Berry

Accepted for the Council:

Anne Mayhew
Vice Chancellor and
Dean of Graduate Studies

(Original signatures are on file with official student records.)

Monte Carlo Simulation of Scatter in a Cone-beam X-ray Micro-CT Scanner

A Thesis

Presented for the

Master of Science Degree

The University of Tennessee, Knoxville

Noel F. Black

May 2005

Acknowledgments

This research supported by NIH grant ROI-EB00789. Thanks to Shawn Gleason, Mike Paulus, and the staff at ImTek, Inc., for help with data acquisition. Thanks to Thomas Benson for mouse reconstruction data. Thanks to Thomas Benson and Geoff Mazeroff for many helpful conversations.

Contents

List of Figures

Chapter 1

Introduction

The acceptance of scattered radiation in the projection data of x-ray computed tomography (CT) imaging causes inaccuracies in measured attenuation coefficients, which reduces the quality of the reconstructed image. Specifically, it degrades the low-contrast detectability [5] and causes the appearance of cupping and streak artifacts [10, 12, 6]. The effect depends strongly on the type of scanner and the object being imaged. Monte Carlo simulation is the preferred method for studying particle transport; it has been used previously to estimate scatter in conventional diagnostic CT (as opposed to micro-CT, which is used for small animal imaging) and also in PET and SPECT [3] [15] [17] [20] [27]. Most of the previous CT studies simulated the pencil-beam or fan-beam geometries. Beekman and collaborators [4] have found that scatter profiles in cone beam micro-CT are smooth but not uniform, and in [31] they propose an iterative scatter correction scheme based on Monte Carlo simulation. This method is basically the same as that already used in PET and SPECT. It takes the scatter-contaminated reconstruction as the zeroth-order image. The Monte Carlo code simulates scatter on this reconstruction, and the scatter projections are then incorporated to obtain a scatter-corrected reconstruction. The reconstruction may be obtained either with analytical (Feldkamp) or statistical (Ordered Subsets Convex, OSC) algorithms. In the analytical reconstruction, the scatter projections are simply subtracted from the original projection data. In the statistical case, the scatter projections are incorporated as background terms in the update equation.

We have written a Monte carlo simulation code, independent of any other existing code, to calculate the scatter to primary ratio S/P of detected radiation in a particular micro-CT scanner. The Beekman group has reported S/P values of $5-10\%$ in micro-CT, rising to 100% for high density objects. We want to determine the magnitude and effect of scatter contamination in cone beam micro-CT, taking the MicroCAT tomograph [22] from ImTek, Inc. (Knoxville, TN, USA) as our prototype scanner. In particular, we are interested in S/P for objects of practical interest in clinical research, namely laboratory mice. If the magnitude of the detected scatter is non-negligible then scatter correction is necessary for quantitative micro-CT imaging.

We first discuss the physics involved, including x-ray production at the source and photon transport in the scanned object. We next describe how the physics is implemented in the Monte Carlo code. The simulation is then compered to the results of a validation experiment using the beam stop method, with Lucite blocks as the scattering object. Finally, we simulate scattering on a mouse object. The magnitude of S/P for this object will indicate whether scatter correction is necessary in practice for quantitative imaging. We then compare the results of mouse objects thresholded with five component materials (air, water, soft tissue, muscle, and bone) with results from single component mouse objects. If the scatter from a five-component mouse object is nearly the same as that from a mouse object composed entirely of water or soft tissue, for example, then we need only simulate scattering on the simpler object to make scatter corrections.

Chapter 2

Physics of Photon Transport

2.1 Overview

X-rays are emitted from the source and illuminate the object. An x-ray photon which enters the object to be imaged may be absorbed or scattered (or both), or may pass through without interacting. A fraction of the radiation emerging from the object will hit the detector. The modern CCD detectors have a response that is very nearly energy independent and proportional to the photon flux (i.e. they are nearly ideal) [13] [16] [29]. We therefore confine our attention to the physics of the x-ray beam and of photon transport in the object. Our simulation assumes that all photons incident on the detector are actually detected.

2.2 X-ray Source

X-rays are generated at the source with an energy spectrum characteristic of the anode material, which is commonly tungsten, and the anode potential. The energy spectrum has the general shape of a broadly peaked distribution between 0 and a cutoff equal to the maximum energy attainable by an electron accelerated through the anode potential, with peaks superposed at characteristic edge energies. The diagnostic energy range typically lies below 100 keV.

When electrons are accelerated in the x-ray tube through the anode potential and bombard the anode, they scatter off the atomic electrons and nuclei. Most (roughly 99% for anode potentials below 1 MeV) lose energy little by little in a series of glancing collisions, eventually diffusing into the anode. The rest contribute radiation to the x-ray beam by one of two mechanisms: bremsstrahlung or atomic transition. Bremsstrahlung is the radiation directly produced by the acceleration of a charged electron during a collision. It has a continuous spectrum with wide distribution of energies and the general shape of a broad peak, with a maximum energy equal to the kinetic energy of the bombarding electrons. This energy in keV is numerically equal to the peak anode potential in kVp, which is the usual unit since the anode potential is commonly obtained from an AC source. The second mechanism begins with the ionization of an anode atom. The incident electron ejects an inner shell atomic electron, typically from the K or L shell. An outer electron then drops to fill the vacancy, losing a photon with characteristic energy equal to the energy difference between the atomic levels.

The resulting x-ray spectrum is a superposition of the continous bremsstrahlung spectrum and the characteristic lines from atomic transitions. Approximately equal numbers of electrons lose energy by each of these mechanisms, but the bremsstrahlung radiation is directional whereas the characteristic radiation is isotropic. The bremsstrahlung intensity is greatest in directions perpendicular to the acceleration vector of the scattering electron. The relative beam composition can therefore be controlled somewhat by the direction of collimation. The ideal x-ray beam for imaging would be monoenergetic. In practice it should be as uniform as possible. Imaging therefore favors the continuous spectrum, so the beam is collimated so as to maximize this component. In addition, the beam is filtered through a thin (on the order of 1 mm) slice of aluminum, which removes characteristic lines from the low energy end where they dominate the spectrum.

Tungsten anode energy spectra at 50 kVp and 80 kVp are well simulated in Fig. (2.1). The theoretical spectra are generated from the TASMIP code of Boone and Seibert [1], which polynomially interpolates measured constant potential tungsten anode x-ray spectra at 1 keV intervals. The K_α and K_β lines are obvious in the 80 kVp spectrum at approximately 59 and 68 keV, respectively.

The focal spot size can be controlled by collimation and by the angle of the anode surface with respect to the electron beam. The spatial intensity distribution and the geometrical shape of the beam, which is determined by collimation, are the other factors specifying the nature of the source x-rays .

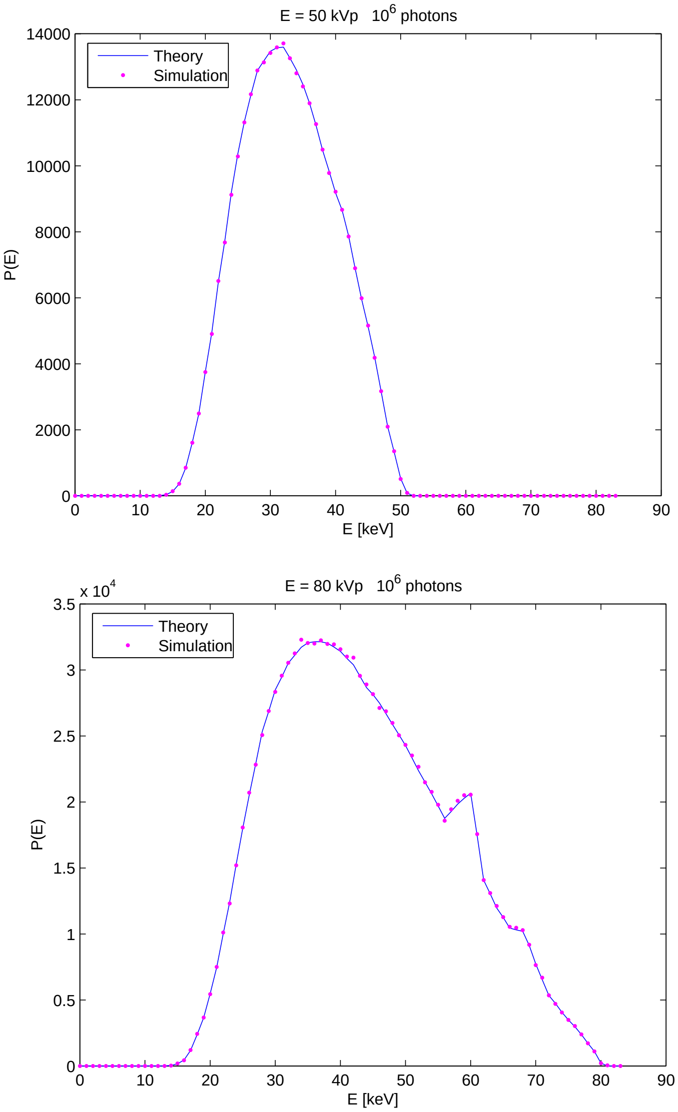

Figure 2.1: Tungsten anode x-ray energy spectrum at a) 50kVp and b) 80 kVp

2.3 Attenuation Lengths

The intensity $I(d)$ of primary radiation decreases exponentially with distance d in traversing a material with density ρ and total attenuation coefficient μ_{tot} as

$$I(d) = I_0 \, e^{-\rho \mu_{tot} d}. \tag{2.1}$$

The dominant interactions of radiation in matter at energies below 1 MeV are photoelectric absorption, coherent scattering, and incoherent scattering. Neglecting the subdominant interactions (electron-positron production in the fields of the nucleus and of the atomic electrons, and the photonuclear interactions), the total attenuation coefficient is given as the sum $\mu_{tot} = \mu_{pe} + \mu_{coh} + \mu_{incoh}$. Our code uses the attenuation coefficients of the XCOM code at NIST [21]. Fig. (2.2) shows the photon attenuation coefficients for Lucite (polymethyl methacrylate, also known as plexiglass.) The photon attenuation and scattering properties of Lucite are very similar to those of soft tissue, so it is a commonly chosen tissue equivalent phantom material. Fig. (2.3) compares the theoretical exponential attenuation of a pencil beam of 40 keV photons in Lucite with the results of the simulation. A linear fit of the simulation points correctly reproduces the total attenuation coefficient $\mu_{total} = 0.235$ cm^2/g. Fig. (2.4) compares the theoretical exponential attenuation by scattering with scattering attenuation coefficient $\mu_{scatt} = \mu_{coherent} + \mu_{incoherent} = 2.02$ cm^2/g to the simulation results, also at 40 keV. S' here is the number of photons that has scattered at least once. For small Lucite

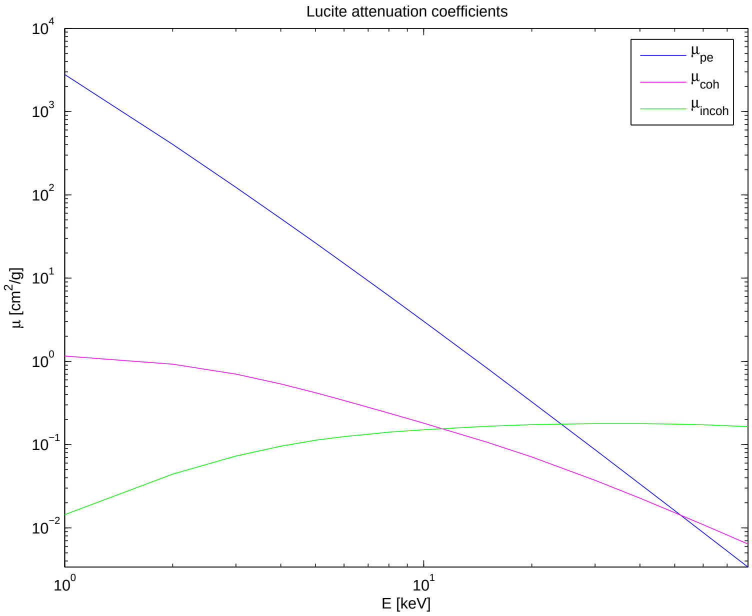

Figure 2.2: Lucite attenuation coefficients

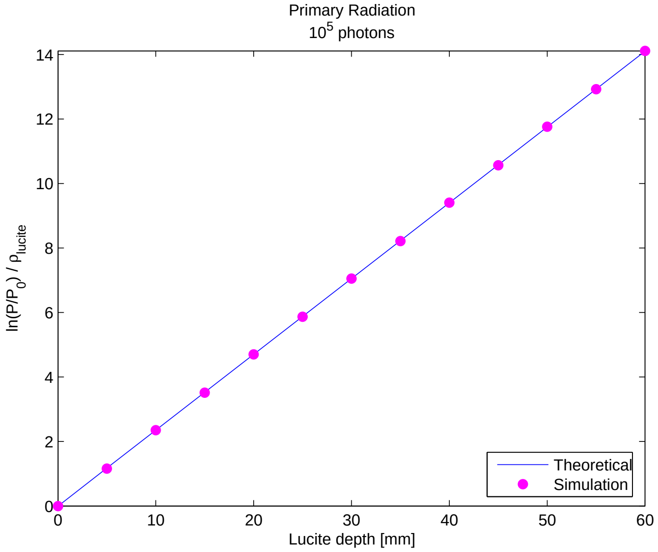

Figure 2.3: Total attenuation of 40 keV monoenergetic x-rays in Lucite

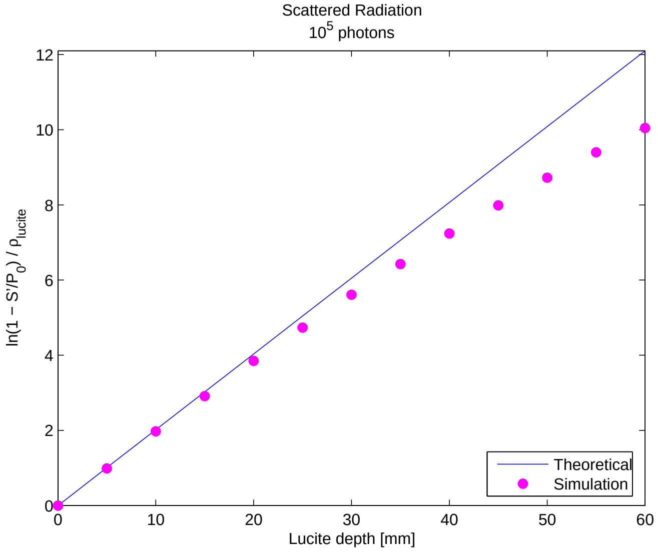

Figure 2.4: Attenuation of 40 keV monoenergetic x-rays by scattering in Lucite. The theoretical curve corresponds to the total number of scatters, whereas the simulation curve refers to the number of scattered photons. The departure with greater Lucite depth indicates the onset of multiple scattering.

depths, the simulation follows the theoretical curve, indicating that multiple scattering is negligible here. The departure at larger Lucite depths thus indicates the onset of multiple scattering. It has been verified that by counting the total number of scatter interactions in the simulation, instead of the number of scattered photons as is shown in Fig. (2.4), and using the photon path length as the Lucite depth, the theoretical curve is accurately reproduced.

2.4 Photoelectric Absorption

A photon interacting with an atom by the photoelectric effect is completely absorbed and ejects an atomic electron accompanied by a small intensity of flourescence x-rays. These flourescence x-rays have energies below 5 keV for low-Z elements typical of soft tissue and tissue equivalent materials like water and Lucite. Photoelectric absorption is the dominant interaction at low photon energies (below about 25 keV in these materials.)

2.5 Coherent Scattering

A coherently scattered photon is elastically scattered at an angle θ (relative to its direction before scattering) with a distribution given by the coherent scattering differential cross section:

$$\left(\frac{d\sigma}{d\Omega}\right)_{coh} = \frac{r_e^2}{2}(1 + cos^2(\theta))F_m^2(x) \tag{2.2}$$

where r_e is the classical electron radius, $F(x, Z)$ is the atomic form factor for the element of atomic number Z, and x is the momentum transfer variable. The form factor depends on the angle θ and energy E of the scattered photon only through the combination given by the momentum transfer variable:

$$x = \frac{E}{hc} sin(\theta/2) \tag{2.3}$$

where $hc = 1.239841857 keV nm$. This cross section is the product of the material-independent Thomson differential cross section

$$\left(\frac{d\sigma}{d\Omega}\right)_{Thomson} = \frac{r_e^2}{2}(1 + cos^2(\theta)) \tag{2.4}$$

and the square of the atomic form factor $F_m(x)$.

The atomic form factor accounts for the interference between the atomic electrons, and dominates the angular distribution. The square of the molecular form factor is often calculated as the sum of the squares of atomic form factors weighted by the relative atomic abundances n_i in the molecule:

$$F_{mol}^2(x) = \sum_i n_i F^2(x, Z_i). \tag{2.5}$$

This ‘free gas model’ or ‘independent atomic model’ (IAM) assumes each atom scatters independently of its neighbors. It does not take into account the collective molecular interference effects of atoms within the molecule and between atoms in closely spaced molecules, and is inadequate at small momentum transfer [23].

Johns and Yaffe [11] showed that the (IAM) form factors do not correctly predict the scattering distribution of x-rays on water, which was measured by Narten [18] and Narten and Levy [19] for 17.4 keV x-rays from a molybdenum source between $x = 0.4$ and 12.7nm^{-1}. They found that the measured molecular form factors were required for agreement. The main effect of using these measured form factors is to shift the peak of the distribution slightly away from 0° (from the forward direction) and to superimpose diffraction peaks on the smooth IAM distribution. These diffraction peaks become very pronounced in the distributions of highly ordered materials, for which the IAM description breaks down. The IAM and measured distributions agree in the limit of large momentum transfer. Since the scattering distributions of most tissues appear very similar to water [14], it is expected that the measured molecular form factors should be used for a quantitative simulation of scattering in CT imaging. Our code uses the measured molecular form factors of [23] for Lucite and water. Molecular form factors for other materials are formed from equation 2.5 using the atomic form factors of Hubbel, *et al.* [7].

Coherent scatter dominates incoherent scatter at low energies (below about 10 keV). Even though the $\mu_{coherent} < \mu_{incoherent}$ above this, there are two reason why coherent scatter is expected to be important in the simulation. First, coherent scatter strongly dominates incoherent scatter in the forward direction. Since the CT scanner detector will be essentially in the forward direction, an accurate description of coherent scattering, especially for small momentum transfer, is crucial. Second, as the energy of a coherently scattered photon is unchanged, it is not any more likely to be absorbed after scattering than before. An incoherently scattered photon generally loses energy by scattering and is therefore more likely to be absorbed after scatter (and therefore not be detected) since μ_{pe} increases with decreasing photon energy.

The angular distributions for coherent scattering at three different energies within the relevant energy range are shown in Fig. (2.5), and the simulations agree very well with theoretical expectations.

2.6 Incoherent Scattering

The angular distribution of an incoherently scattered photon is given by

$$\left(\frac{d\sigma}{d\Omega}\right)_{incoh} = \frac{r_e^2}{2}\left(\frac{E'}{E}\right)^2\left(\frac{E'}{E}+\frac{E}{E'}+cos^2(\theta)-1\right)S_m(x) \tag{2.6}$$

which is the product of the Klein-Nishina formula

$$\left(\frac{d\sigma}{d\Omega}\right)_{Klein-Nishina} = \frac{r_e^2}{2}\left(\frac{E'}{E}\right)^2\left(\frac{E'}{E}+\frac{E}{E'}+cos^2(\theta)-1\right) \tag{2.7}$$

and the incoherent scattering function $S_m(x)$. Here E and E' are the energies of the incoming and scattered photons, respectively. The scattered photon transfers energy and momentum to an atomic electron in the collision and emerges with energy E' given

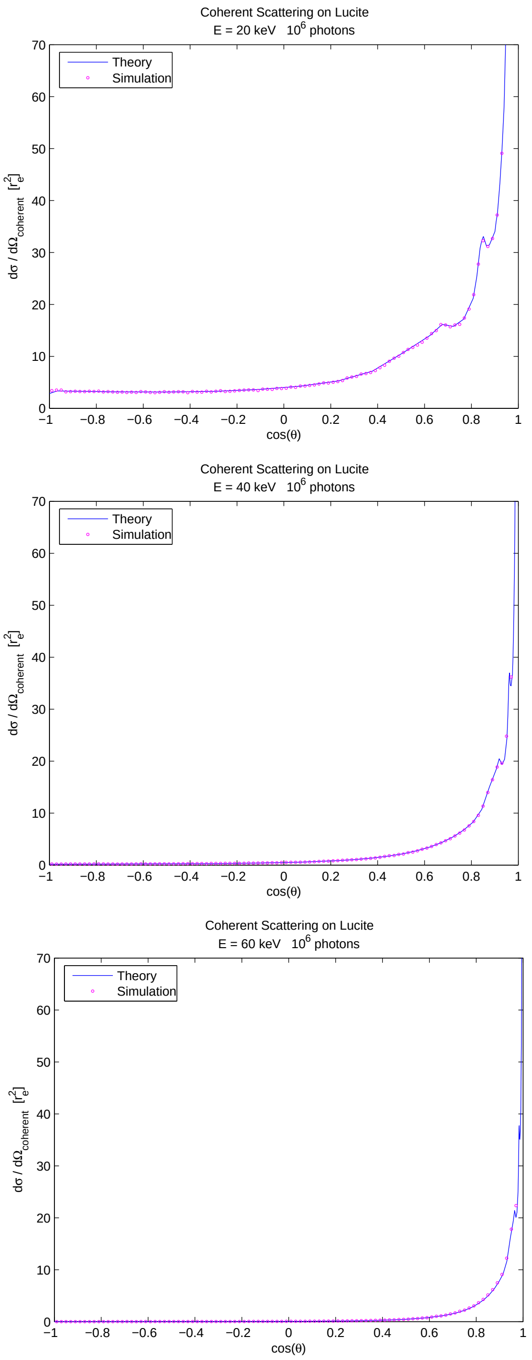

Figure 2.5: Coherent scattering distributions of monoenergetic x-rays in Lucite.

by

$$E' = E/[1 + (E/m_e c^2)(1 - cos(\theta))], \tag{2.8}$$

which merely states energy conservation for the interaction. The Klein-Nishina formula describes the angular distribution of photons incoherently scattered from free electrons [9]. It breaks down for photon energies comparable to the binding energies of the inner shell atomic electrons. The magnitude of the scattering function is essentially a measure of this binding energy [25]. Incoherent scattering is not a collective effect, so in this case the molecular scattering function is expected to be accurately constructed as the sum of atomic scattering functions weighted by the relative atomic abundances:

$$S_{mol}(x) = \sum_i n_i S(x, Z_i). \tag{2.9}$$

Incoherent scattering dominates at energies above about 10 keV.

Our code uses the incoherent scattering functions of Hubbel, *et al.* [8]. Relative atomic abundances for muscle, soft tissue, and bone (used in the mouse simulation) are taken from XCOM [21]. The angular distributions for incoherent scattering at three different energies within the relevant energy range are shown in Fig. (2.6), and the simulations agree very well with theoretical expectations. Fig. (2.7) compares the energy distribution of incoherently scattered photons with theoretical expectations, and again the agreement is very good.

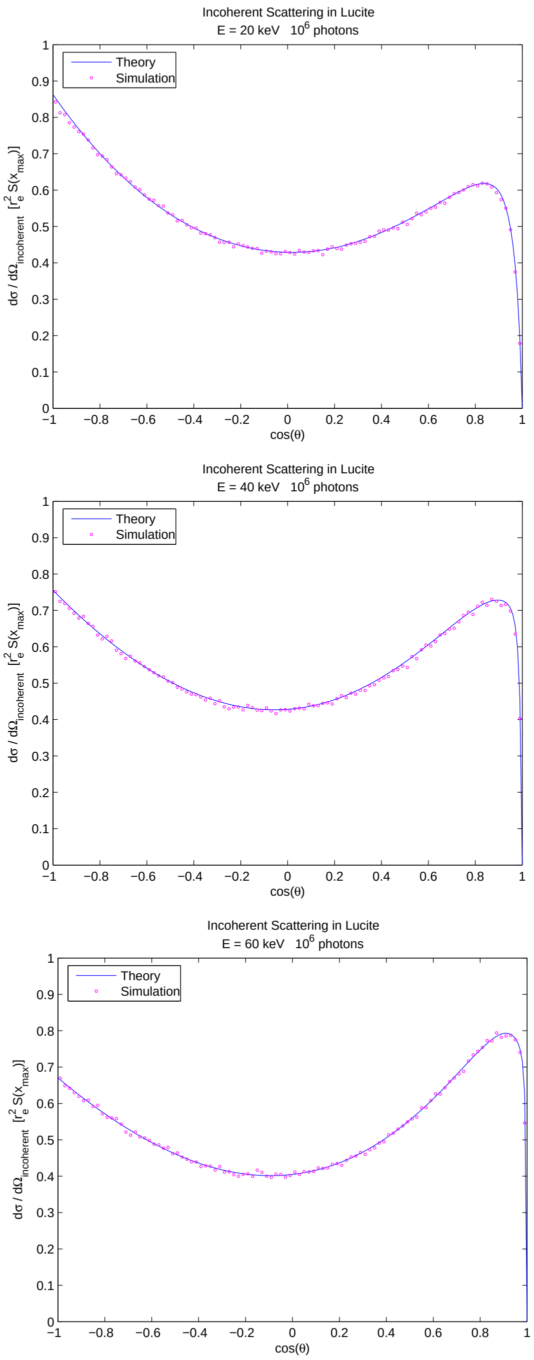

Figure 2.6: Incoherent scattering distributions of monoenergetic x-rays in Lucite.

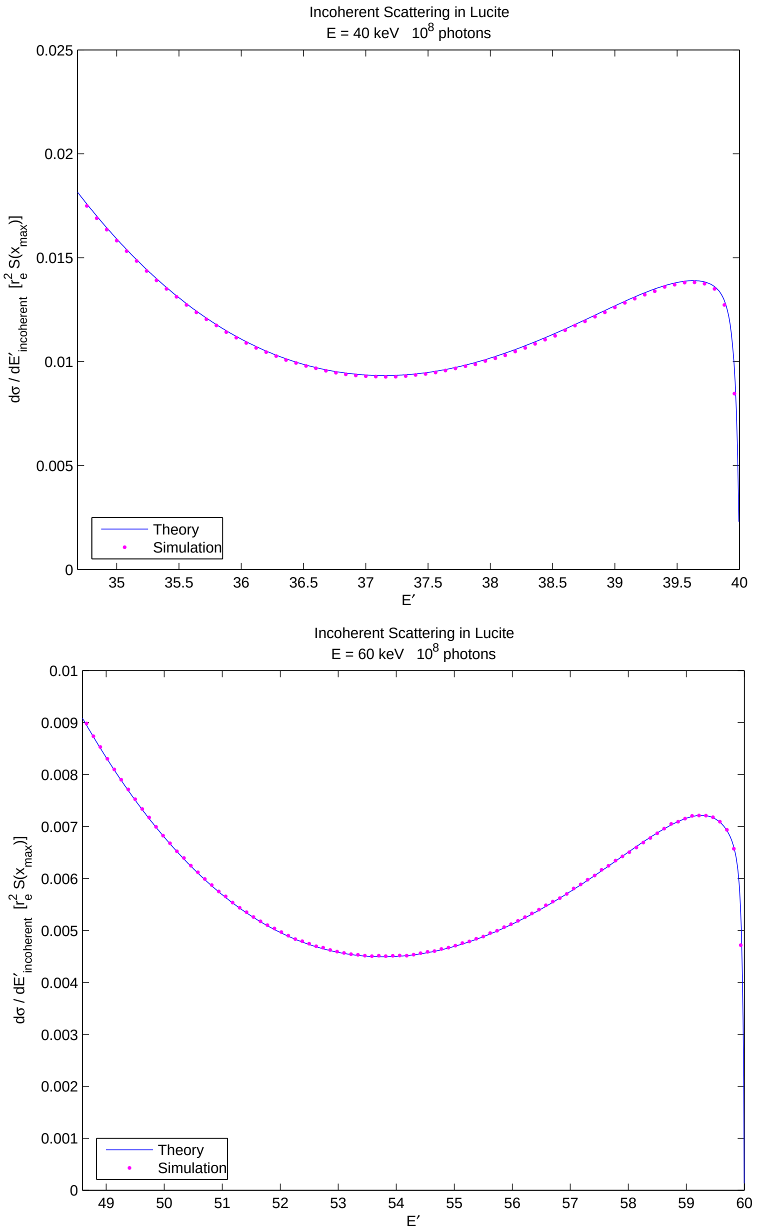

Figure 2.7: Energy distribution of Compton scattered photons at a) 40kVp and b) 60 kVp

2.7 Geometry

There are several coordinate systems in use, connected by rotation matrices. One sytem is fixed in the laboratory frame of reference, one system is fixed in the scanner and rotates with it around the object to obtain tomographic projections, and one system is the frame of reference of the current photon. This last system is the reference system for the angular probability distributions when the photon scatters in a new direction. As evidence that the geometry has been coded correctly, Fig. (2.8) shows the projection of the scatter component of a 80 kVp pencil beam of photons incident on a 30 mm thick Lucite block. The result is intuitively what one would expect. The beam is aimed off center to so that any errors in geometrical transformation between the photon coordinate system and the scanner coordinate system might be revealed. The azimuthal independence is apparent. Also apparent is the intensity suppression in the exact forward direction and the intensity peak in the near forward direction.

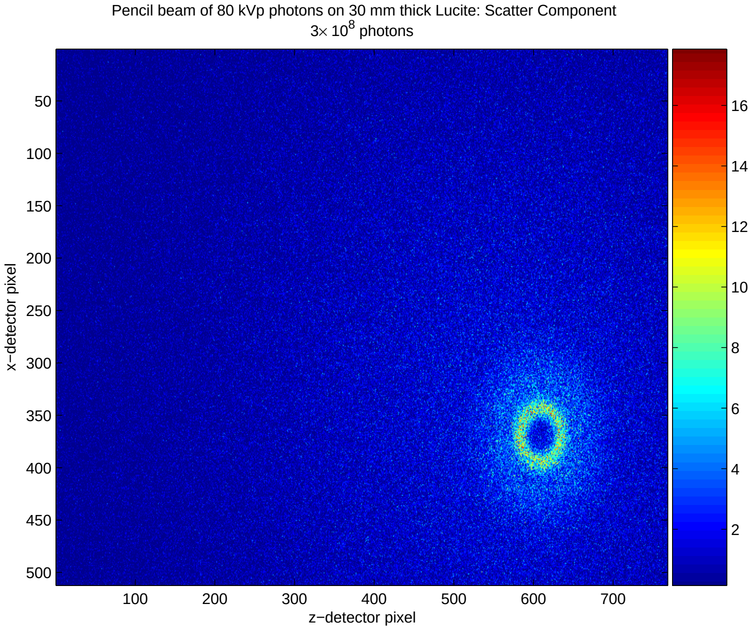

Figure 2.8: The projection of the scatter component of a 80 kVp pencil beam of photons incident on a 30 mm thick Lucite block.

Chapter 3

Description of the Monte Carlo Program

3.1 Random Number Generation

Monte Carlo simulation requires large quantities of high quality (pseudo-)random numbers, so it is important to use a random number generator that has passed a number of statistical tests of randomness and that has a large enough period. We consider the simulation of the validation experiment, described below, to estimate the number of random numbers needed by the code. That simulation uses 600M photons per projection with a $512 \times 512 \times 768$ voxel space. Each photon requires three random numbers to determine its initial energy and direction. At each voxel, one random number determines which interaction occurs, and if the interaction is either coherent or incoherent scatter, then two more are needed to determine the outgoing direction. If a photon traverses a number of voxels on the order of 1000 and if we assume, to obtain an upper limit, that the interaction at each voxel is a scatter, then there may be

$$\begin{gathered} 600M(\text{photons}) \\ \times 3(\text{initial energy, angles}) \\ \times 1000(\text{voxels}) \\ \times 2(\text{scatter angles}) \\ = 3.6 \times 10^{11} \end{gathered} \tag{3.1}$$

random numbers per projection. If there are 360 projections, as may be required for tomographic imaging, then

$$360 \times 3.6 \times 10^{12} = 1.3 \times 10^{15} \tag{3.2}$$

uncorrelated random numbers are necessary. This code uses the combined multiple recursive generator of the SPRNG [28] library. Its period of approximately $2^{219} \approx 10^{66}$ is expected to be large enough for our simulation. Only if the number of photons or the voxel space dimensions were increased by orders of magnitude would a generator with a greater period be needed. The combined multiple recursive generator is defined by

$$z(n) = x(n) + y(n) \cdot 2^{32} \bmod 2^{64} \tag{3.3}$$

where $y(n)$ is the sequence generated by the following prime modulus multiple recursive generator

$$y(n) = 107374182 \cdot y(n-1) + 104480 \cdot y(n-5) \bmod 2147483647 \tag{3.4}$$

and $x(n)$ is the sequence generated by the 64 bit linear congruential generator

$$x(n) = a \cdot x(n-1) + p \bmod 2^{64}. \tag{3.5}$$

Here a is a multiplier set during initialization and p is a prime number. Different ps produce reasonably independent streams of random numbers. The random number generator returns the 31 high order bits of $z(n)$. Each node in the parallelized code uses its MPI rank as the seed, i.e. the starting point for the generator. The SPRNG library, designed to be scalable and portable to a large variety of architectures, was developed especially for large scale Monte Carlo calculations.

3.2 Description of the Code

The Monte Carlo code tracks each photon from production at the source until it is absorbed in the object or leaves the voxel space of the object and is either detected or misses the detector. The energy E of a source photon is determined by random sampling of the energy distribution $P(E)$. A random number ξ with a flat distribution on the interval $[0,1)$ determines E from

$$\xi = \int_0^E P(E)\, dE \;\; / \int_0^\infty P(E)\, dE \tag{3.6}$$

by the inversion method [24] . The focal spot is taken to be a point, from which the photon emanates with a direction sampled from the angular distribution of the x-ray beam. This distribution must be measured in the actual scanner to be simulated. Photons are assumed to have no interactions in the air surrounding the voxel space, so the direction of the source photons determines its entry point into the voxel space and its direction at that point.

Each voxel is labled with a material type by the material map that specifies the geometrical location and composition of the object in the voxel space. A material type specifies a density and a set of characteristic attenuation coefficients for the three interactions, which determine the interaction probabilities in the voxel, and characteristic form factors $F_m(x)$ and scattering functions $S_m(x)$ which determine the angular distributions of photons scattered in the voxel. The size of the voxel space is determined by the scanner geometry, which is specified by the detector dimensions L_x^{det} and L_z^{det} and the distances L_{SD} between the source and detector and L_{SC} between the source and center of rotation of the scanner. The scanner-fixed coordinate system referred to is right handed with origin at the center of rotation, the center of the detector in the $\hat{y}$ direction, and the scanner rotation axis in the $\hat{z}$ direction. The voxel space dimensions L_x^{vox}, L_y^{vox}, andL_z^{vox} are determined such that the voxel space fully intersects the solid angle formed between the source point and the detector. The voxel dimensions w_x^{vox}, w_y^{vox}, w_z^{vox} are determined from the voxel space dimensions and from the user input resolution $N_x^{vox} \times N_y^{vox} \times N_z^{vox}$.

The path length d of the photon trajectory through the voxel is computed with an algorithm that appears essentially equivalent to the one proposed by Siddon [26]. The probabilities $P(i), i = 0...3$ for the photon to have each of the three possible interactions (photoelectric absorption, coherent scatter, and incoherent scatter) or no interaction are computed as

$$P(i) = (1 - e^{-\rho_i \mu_i d}) \prod_{\substack{j=0,3 \\ j \neq i}} e^{-\rho_j \mu_j d} / N \tag{3.7}$$

where N is a normalization factor. The interaction in the voxel is then determined by random sampling.

If the photon is absorbed by the photoelectric effect, its history ends. The flourescence x-rays are not traced, as their energies are below 5 keV for the low-Z tissue equivalent materials. 5 keV is taken as the low energy cutoff; a photon with energy less than 5 keV is assumed to be absorbed.

If the photon scatters coherently, it is scattered from the center of the path within the voxel at an angle $\theta \in [0, \pi]$, relative to its incoming direction, determined by sampling the coherent scattering differential cross section $\left(\frac{d\sigma}{d\Omega}\right)_{coh}$ and at azimuthal angle $\phi \in [0, 2\pi)$ sampled from a flat distribution. θ is determined using the generalized rejection method of Carter and Cashwell [2], which regards $\left(\frac{d\sigma}{d\Omega}\right)_{coh}$ as the product of two probability distributions $\left(\frac{d\sigma}{d\Omega}\right)_{Thomson}$ and $F_m^2(x)$. x is first determined by sampling $F_m^2(x)$ with the inversion method:

$$\xi = \int_0^x F_m^2(x)\, dx \;\; / \int_0^{x_{max}} F_m^2(x)\, dE \tag{3.8}$$

where $x_{max} = E/hc$. The corresponding angle θ (equation 2.3) is then accepted with probability $\left(\frac{d\sigma}{d\Omega}\right)_{Thomson}$. The photon history then continues at the same energy and with the new direction and position.

The incoherent interaction is handled like the coherent interaction with $\left(\frac{d\sigma}{d\Omega}\right)_{Compton}$ and the scattering function $S_m(x)$ in place of $\left(\frac{d\sigma}{d\Omega}\right)_{Thomson}$ and the square of the form factor $F_m^2(x)$, respectively. In addition, the energy E' of the scattered photon differs from the energy E of the incoming photon according to equation 2.8. If $E' > 5$ keV the photon history continues with the new energy; if $E' < 5$ keV the photon is assumed to be absorbed and its history ends.

A photon is tracked until its history ends or until it leaves the voxel space. If it exits the voxel space, its exit point and direction determine which detector cell it hits or whether it misses the detector. The detector is divided into cells according to the user input detector $N_x^{det} \times N_y^{det} \times N_z^{det}$. A photon that hits a detector cell is assumed to be detected there. The output of the code is the distribution of detected primary and scattered radiation, and the total numbers of absorbed photons, scattered photons, and photons that missed the detector. For tomographic simulation, the source is rotated about the rotation axis in small increments and a projection made from each viewpoint.

The Monte Carlo code is written in C, with many Matlab scripts for pre- and postprocessing (e.g. map thresholding, data assimilation and analysis, etc.). The input attenuation map is stored as an array of short integers. The results are arrays the size of the detector space containing the number of scattered and primary photons collected at each detector cell and are stored as integers. The probability distributions are accessed by table lookup and inverted by linear interpolation. The table for a distribution $P(x)$ contains columns for the independent variable x, the distribution $P(x)$, and the cumulative distribution $\tilde{P}(x) = \int_{x_0}^{x} P(x)\, dx$. The value x selected by a random number ξ is determined by first finding i from the table such that $\tilde{P}(x_{i-1}) < \xi < \tilde{P}(x_i)$. x is then found by linear interpolation of $P(x)$, which amounts to quadratic interpolation of $\tilde{P}(x)$. This is important, since linearly interpolating $P(x)$ directly leads to a stair-step pattern in the simulation data. The compute time scales approximately linearly with the number of photons and the sizes of the voxel and detector spaces.

Chapter 4

Validation

4.1 Validation Experiment

Experimental projections were made of phantoms composed of Lucite slabs and lead stops in a CT micro-scanner. The rotation axis is horizontal in the scanner, and the projection angle was chosen so that the beam axis was vertical with the x-ray source was at the high side and the detector at the low side. With this arrangement a Lucite block may rest in the sample bed with the lead placed on top of the Lucite, nearer to the source. The Lucite was cut into blocks of various thicknesses with 90×60 mm^2 area perpendicular to the beam axis, which is chosen large enough that all of the beam intersects the phantom. Lead of thickness 1.59 mm was cut into small, somewhat square pieces of various sizes (the sizes are given as approximate edge dimension) to serve as stops. Since a lead stop should stop most of the radiation incident upon it, most of the radiation detected behind it in the shadow region should have been scattered there from the Lucite.

The scanner had a tungsten anode x-ray source and was operated at an anode voltage of 80 kVp and an anode current of 500 μA. The exposure time was 375 μs. The source to detector distance $L_{SD} = 359.68$ mm and the source to center of rotation distance $L_{SC} = 274.52$ mm. The effective dimension of a detector cell $w_{det} = .16176$ mm, with a binned resolution of 512×768 cells.

Fig. (4.1) compares the experimental results with those of the simulation for an 80 kVp x-ray beam scattering on a 12.0 mm thick Lucite slab with lead stops of size 4mm, 6mm, 8mm, and 10mm on a line through the projection of each stop. The experimental projections of the stops have noticeably rounded edges compared with the simulated projections. This is probably due to two main effects. First, the focal spot size of the real x-ray beam is finite, whereas the simulation regards it as a point. A finite focal spot size will blur edges. Second, the lead pieces are not precisely of uniform thickness; the edges become crimped and distorted when the stops are cut out, since lead is a very soft material and precision machining was not possible. The agreement is therefore expected to be better for larger size stops, for which the rounded experimental edges on opposite sides of the stop are nonoverlapping, and this trend is clearly evident in Fig. (4.1).

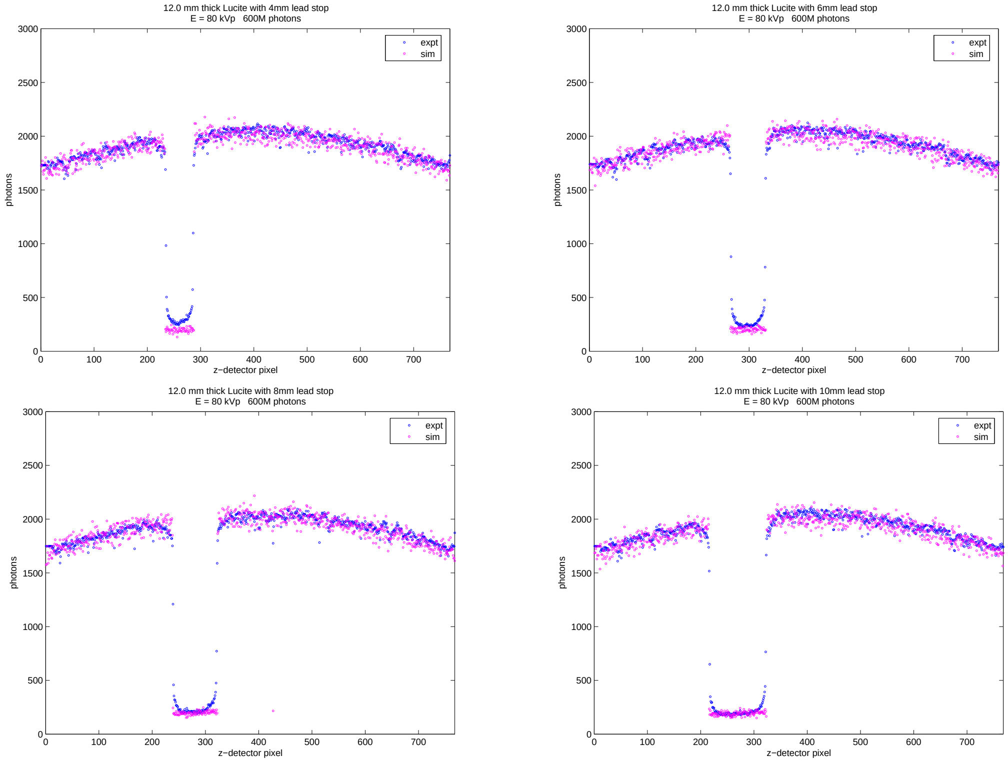

Figure 4.1: Comparison of experimental and simulation results for 80 kVp beam illuminating a 12.0 mm thick Lucite slab with lead stops of size a) 4mm, b) 6 mm, c) 8mm, and d) 10 mm.

If T_S is the intensity of detected radiation behind the lead stop and T_{SP} is intensity of detected radiation in the same region but with no lead stop, the S/P ratio should be given by $S/P = \frac{T_S}{(T_{SP}-T_S)}$ assuming the stop blocks all radiation incident upon it. If a fraction x of the incident primary radiation is unblocked by the stop, then $S/P = \frac{(T_S - xT_{SP})}{(T_{SP}-T_S)}$. (x can be calculated from the attenuation coefficients for lead.) The scatter to primary ratios calculated in this way are plotted in Fig. (4.2) for an 80 kVp beam incident on a 12.0 thick slab of Lucite as a function of lead stop size. A region of interest interior to the lead stop shadow region is selected for tabulation. This region is smaller than the shadow region to avoid edge effects. The agreement is good for the 10 mm stop: S/P$_{expt}$ = 0.0606 and S/P$_{sim}$ = 0.0600. The agreement worsens as the size of the stop decreases, as expected. The relative error is 0.96%, 16.39%, 33.97%, and 52.11% for the 10mm, 8mm, 6mm, and 4mm stops respectively.

Fig. (4.3) plots the simulation results for S/P as a function of Lucite thickness. One set of points tabulates photons over the entire detector and the other set tabulates photons over a small region of interest at the center of the detector. The latter is larger in general for a given Lucite thickness. S/P is just below 0.14 for the 24.0mm thick Lucite block and decreases approximately linearly to zero with decreasing Lucite thickness.

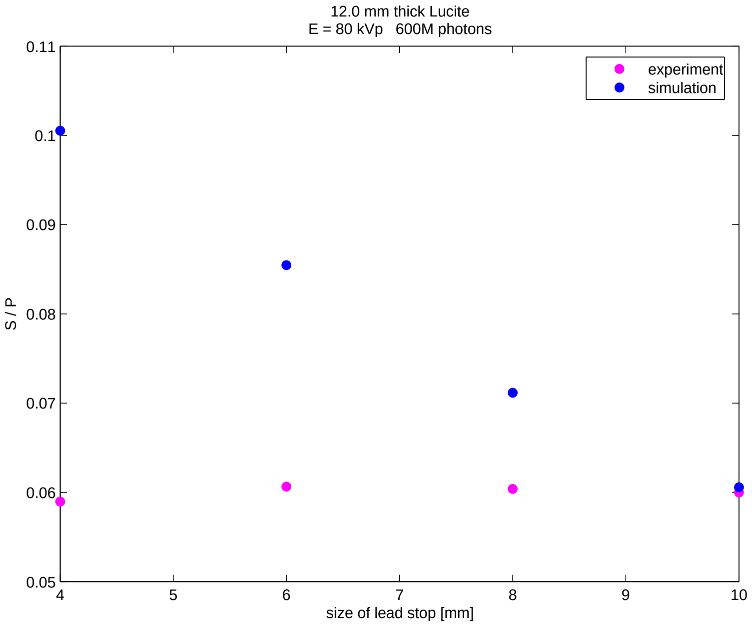

Figure 4.2: S/P ratio for 80 kVp beam scattering on 12.0 mm thick Lucite, as function of lead stop size.

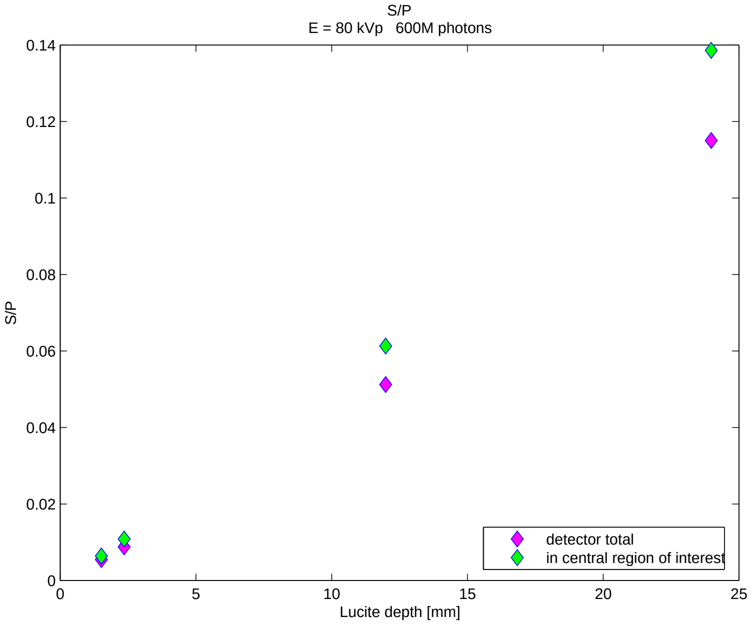

Figure 4.3: Simulated S/P ratio in Lucite

4.2 Simulation on a Mouse Reconstruction

We are interested in the amount of detected scatter in a projection of a typical mouse object. Fig. (4.4) shows a slice of a 256 × 256 × 511 mouse reconstruction. To convert this to an input attenuation map for the simulation each voxel must be labeled as a material type with known attenuation coefficients and scattering properties. A typical mouse is composed primarily of soft tissue, muscle, water, and bone, and is assumed to be surrounded by air. We therefore want to threshold the attenuation map to create an indexed map. Fig. (4.5) shows the plot of a line through the attenuation map with material thresholds superimposed. This line is the x-voxel $= 100$ line of the slice shown in Fig. (4.4); it is approximately the mouse axis and is expected to intersect each of the main mouse component materials as most of it is interior to the mouse. The thresholds are ordered according to their total attenuation coefficients, but their exact placement is basically objective. The results of the simulation are not expected to depend significantly on the exact threshold levels, as the attenuation and scattering properties of water, soft tissue, and muscle are extremely similar. The bone threshold is probably the most significant factor; it also is the most easily placed, using the heuristic that bone should be visible as skull, ribs, and tail in the indexed map. We see in Fig. (4.5) spikes where the skull and tailbone are, an air gap at z-voxel ≈ 420 between the body and the tail, surrounding air at z-voxel $\lesssim 30$ and z-voxel $\gtrsim 450$, and an internal air pocket at z-voxel ≈ 225. These features were considered in placing the low and high thresholds. There appear to be regions of similar intensity I (with some noise) at the

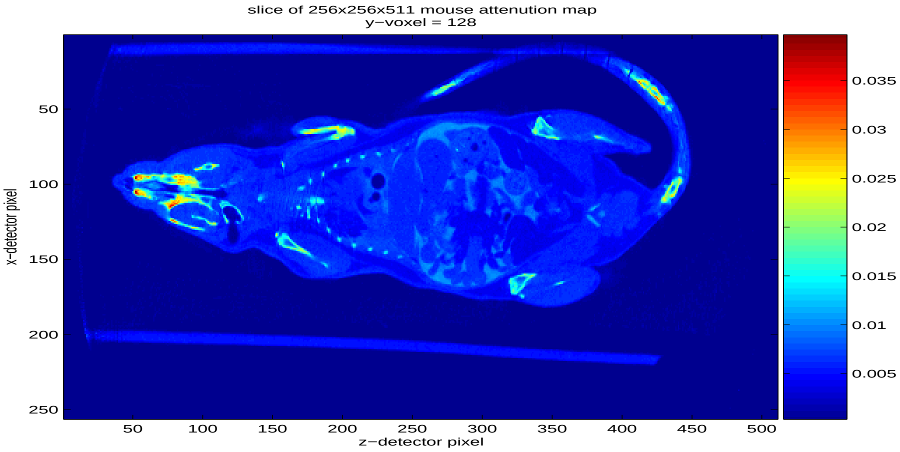

Figure 4.4: Reconstructed mouse.

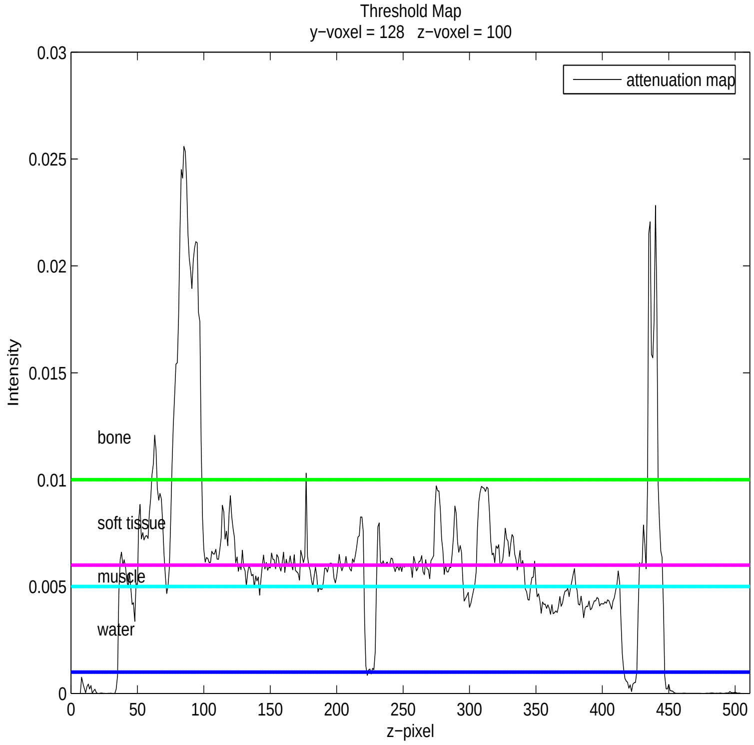

Figure 4.5: Thresholding the mouse.

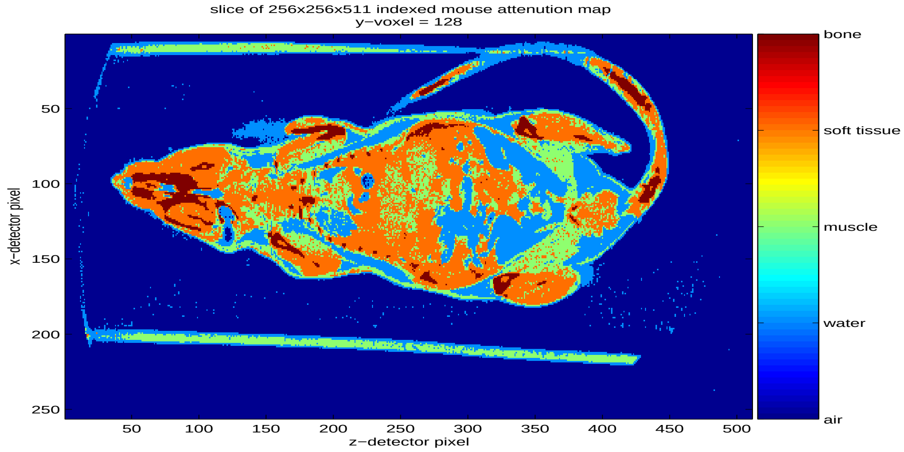

Figure 4.6: Indexed map of the mouse.

intermediate intensities $I \approx .006$ and $I \approx .004$ (arbitrary units), and these influenced the placement of the two intermediate thresholds. Fig. (4.6) shows the resulting indexed mouse map. The skull, ribs, and tailbone are indeed visible as bone and correspond nicely with the same features in the original attenuation map of Fig. (4.4). With this thresholding, the mouse composition turns out to be 0.69% air, 25.42% water, 23.54% muscle, 43.20% soft tissue, and 7.15% bone.

Fig. (4.7) shows the results of the simulation on the indexed mouse attenuation map with two billion photons. The detected primary radiation map embodies a mouse projection that is apparently quite detailed; the skeleton is nicely revealed and small features like the ribs are quite apparent. The detected scattered radiation has the form of a slowly varying bulge roughly centered on the detector, perhaps offset slightly. The primary map is used to segment the mouse from the background, as we are interested in the amount of scattered radiation detected in the region behind the mouse. The scatter

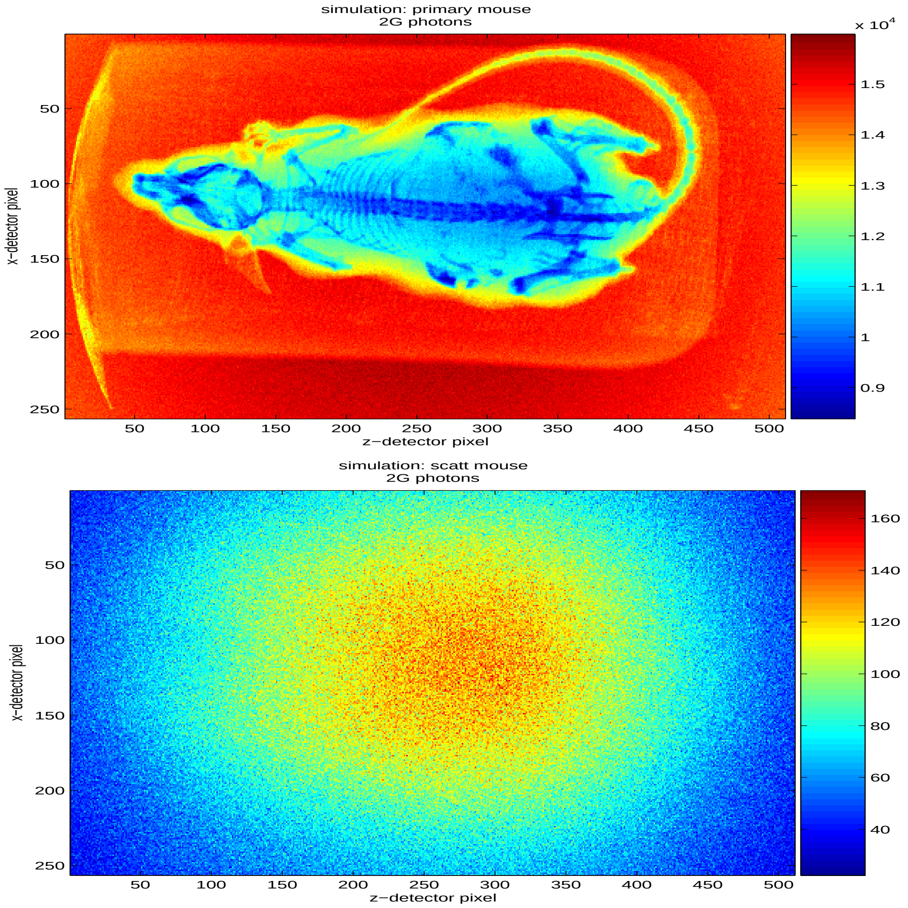

Figure 4.7: Simulated projections of two billion photons on the indexed mouse: a) primary b) scatt

to primary ratio in this region of interest is $S/P = .0097$.

It may not be necessary to index the mouse with five materials in order to estimate the scatter. Since the photon attenuation and scattering properties of soft tissue, muscle, and water are nearly identical, we expect very little difference to result if we index with just three materials - bone, water, and air. We could alternatively simulate scattering on a uniform mouse with a weighted average composition; attenuation coefficients, form factors and scattering functions would be formed as weighted sums with weight coefficients given by the relative abundances of each of the five material types in the mouse. This weighted sum requires interpolation of the material data tables, as the values for different materials are not all specified at the same energies. An even simpler approach is to consider a mouse composed entirely of water. We take this approach as it is expected to differ the most from the five material scheme. Fig. (4.8) shows the results of the simulation with two billion photons on the water mouse. The primary map is now structureless; it shows well the outline of the mouse and indicates the thickness of the mouse in the beam direction. The scatter map looks very similar to that resulting from the five-component mouse. The scatter to primary ratio in the region behind the water mouse is S/P = .0088, slightly less than that for the five-component mouse. Both simulations find an S/P $\lesssim$ 1%, which should be considered quite small in the sense that it is probably not statistically correctable. Fig. (4.9) shows the primary and scatter maps for both mouse objects along the x-voxel = 100 reference line. The primary radiation map for the five-component mouse projection has noticeable structure compared to that for the water mouse, but two primary maps have basically the same shape along this line. The scatter maps for the two mice along the reference line appear very similar, that from the five-component mouse being perhaps slightly larger. Note that the scatter is magnified by a factor of 50 so its form can be seen on the plot.

For comparison, we simulate scattering on two other single-component mice - one composed entirely of bone and the other of soft tissue. Fig. (4.10) compares the primary and scatter maps for the bone mouse, soft tissue mouse, and five-component mouse

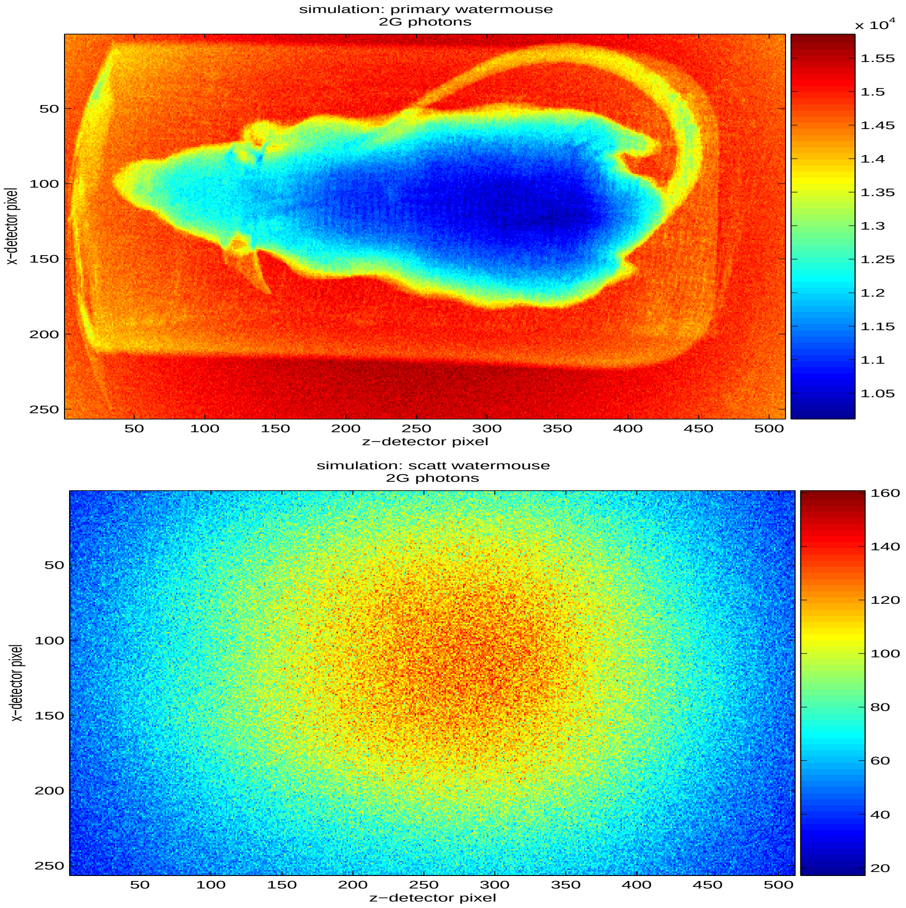

Figure 4.8: Simulated projections of two billion photons on the water mouse: a) primary b) scatt

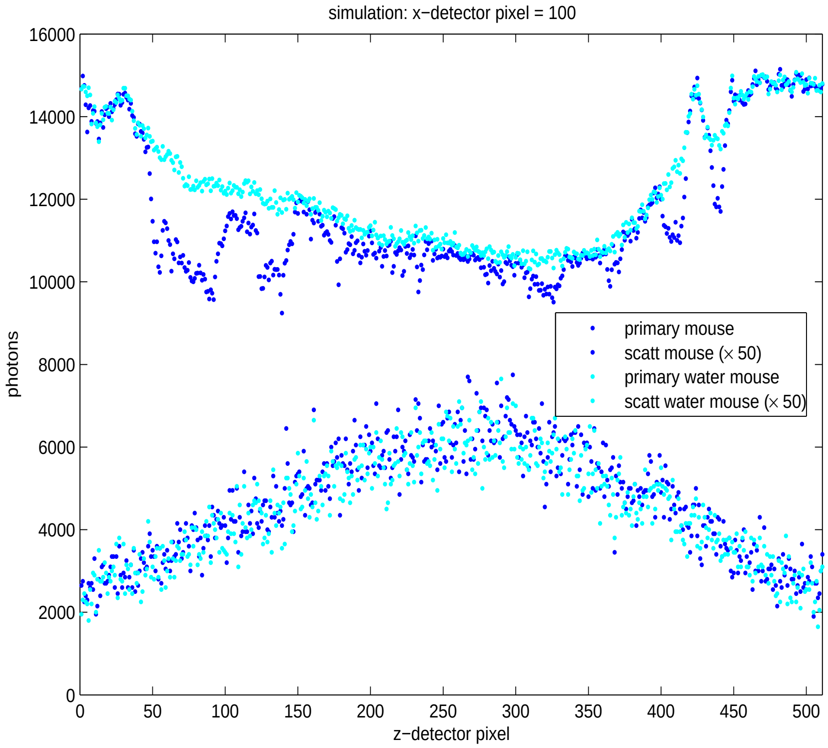

Figure 4.9: Simulation with two billion photons on the five-component mouse and water mouse.

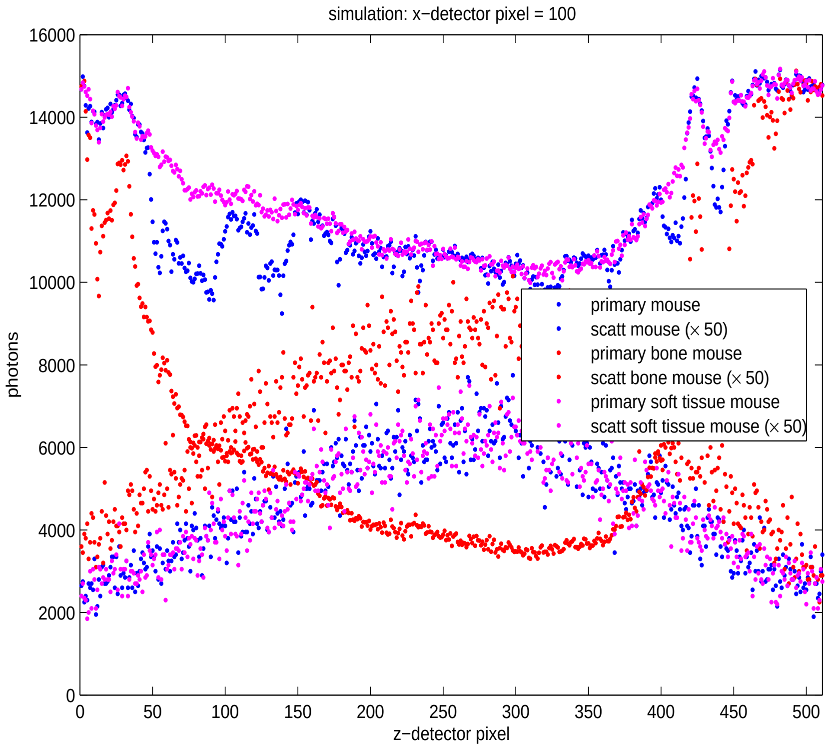

Figure 4.10: Simulation with two billion photons on the five-component mouse, bone mouse, and soft tissue mouse.

objects along the x-voxel = 100 reference line. The results for the soft tissue mouse are very close to those for the water mouse. The plot show clearly that bone is the most strongly attenuating and scattering of the materials considered. The S/P ratio is 0.0287 for the bone mouse and 0.0092 for the soft tissue mouse.

Chapter 5

Conclusions

The scatter to primary ratio in a micro-CT scanner is apparently much smaller than that reported for clinical scanners. While we find that S/P $\lesssim$ 14% for scattering through a 24.0mm thick Lucite block that intersects the beam fully, it is only slightly less than 1% for a typical mouse object. The validation experiment needs to be redone with larger beam stop sizes in order to minimize the problematic edge effects. S/P should then be found by extrapolation to zero stop size. Further, more careful consideration needs to be made of the geometrical shape of the beam and its intersection with the phantom. Our simulation takes the beam to be located inside the solid angle formed between the detector point and the detector. For a object that is fully contained inside the voxel space, this is a fine assumption because no photon outside this region can be scattered to the detector. In the actual validation experiment however, the Lucite blocks did extend outside the voxel space. Photons outside the simulated beam region can scatter back to the detector, increasing S/P_{expt} relative to S/P_{sim}. This is probably not a large effect but should be taken into account, as it is an obvious source of error. The validation is still convincing as it stands since there is agreement with the simulation for the large stop sizes. For these larger stops, the edge effects may be avoided in choosing a region for tabulation of scattered and primary detected photons. Further refinement of the code would take into account the finite focal spot size of the x-ray source. This should blur the edges of beam stops in our simulated projections in a manner similar to that observed in the experimental data.

The scatter to primary ratio small enough that scatter correction, which is inherently statistical, is probably not worthwhile. Future applications of this code could involve untangling beam hardening effects from scatter contamination effects. These two error sources induce very similar artifacts, namely cupping and streaks, and reduction of image contrast. It would also be relatively simple to simulate SPECT imaging by modeling the x-ray source characteristics and detector geometry specific for that modality.

Bibliography

Bibliography

[1] J. M. Boone and J. A. Seibert. An accurate method for computer-generating tungsten anode x-ray spectra from 30 to 140 kv. *Med. Phys.*, 24(11):1661–70, 1997.

[2] L. L. Carter and E. D. Cashwell. *Particle Transport Simulation with the Monte Carlo Method*. TID-26607, ERDA Critical Review Series, U. S. Energy Research and Development Administration, Technical Information Center, Oak Ridge, Tennessee, first edition, 1975.

[3] H. Chan and K. Doi. The validity of monte carlo simulations in studies of scattered radiation in diagnostic radiology. *Phys. Med. Biol.*, 28(2):109–29, 1983.

[4] A. Colijn and F. J. Beekman. Accelerated simulation of cone beam x-ray scatter projections. *IEEE Transactions on Medical Imaging*, 23(5):584 –90, 2004.

[5] M. Endo, T. Tsunoo, N. Nakamori, and K. Yoshida. Effect of scattered radiation on image noise in cone beam CT. *Med. Phys.*, 28(4):469–74, 2001.

[6] G. H. Glover. Compton scatter effects in CT reconstructions. *Med. Phys.*, 9(6):860–7, 1082.

[7] J. H. Hubble and I. Overbo. Relativistic atomic form factors and photon coherent scattering cross sections. *J. Phys. Chem. Ref. Data*, 8(1):69–105, 1979.

[8] J. H. Hubble, W. J. Veigele, E. A. Briggs, R. T. Brown, D. T. Cromer, and R. J. Howerton. Atomic form factors, incoherent scattering functions, and photon scattering cross sections. *J. Phys. Chem. Ref. Data*, 4(3):471–538, 1975.

[9] J. M. Jauch and F. Rohrlich. *The Theory of Photons and Electrons.* Spinger,, Berlin, first edition, 1976.

[10] P. C. Johns and M. Yaffe. Scattered radiation in fan beam imaging systems. *Med. Phys.*, 9(2):231–9, 1982.

[11] P. C. Johns and M. Yaffe. Coherent scattering in diagnostic radiology. *Med. Phys.*, 10:40–50, 1983.

[12] P. M. Joseph and R. D. Spital. The effects of scatter in x-ray computed tomography. *Med. Phys.*, 9(4):464–72, 1982.

[13] Kodak technical bulletin TI0997.

[14] J. Kosanetzky, B. Knoerr, G. Harding, and U. Neitzel. X-ray diffraction measurements of some plastic materials and body tissues. *Med. Phys.*, 14:526–32, 1987.

[15] A. Malušek, M. Sandborg, and G. A. Carlsson. Simulation of scatter in cone beam CT - effects on projection image quality. In *Medical Imaging 2003: Physics of*

Medical Imaging, edited by M. J. Yaffe and L. E. Antonuk, Proceedings of SPIE **5030**, pages 740–51, 2003.

[16] Medoptics corporation, 4588 s. palo verde rd., suite 405, tuscon, az 85714.

[17] N. Meriç, D. Bor, and N. Büget. Determination of scatter fractions of some materials by experimental studies and monte carlo calculations. *Applied Radiation and Isotopes*, 51:161–67, 1999.

[18] A. H. Narten. X-ray diffraction data on liquid water in the temperature range 4 to 200°C. Technical Report ORNL-4578, Oak Ridge National Laboratory, Oak Ridge, TN, 1970.

[19] A. H. Narten and H. A. Levy. Liquid water: molecular correlation functions from x-ray diffraction. *J. Chem. Phys.*, 55:2263–9, 1971.

[20] U. Neitzel, J. Kosanetzky, and G. Harding. Coherent scatter in radiographic imaging: a monte carlo simulation study. *Phys. Med. Biol.*, 30(12):1289–96, 1985.

[21] Photon Cross Sections Database (XCOM.) National Institute of Standards and Technology. http://physics.nist.gov/PhysRefData/contents.html.

[22] M. J. Paulus, H. Sari-Sarraf, S. S. Gleason, M. Bobrek, J. S. Hicks, D. K. Johnson, J. K. Behel, L. H. Thompson, and W. C. Allen. A new x-ray computed tomography system for laboratory mouse imaging. *IEE Trans. Nucl. Sci.*, 46(3):558–64, 1999.

[23] D. E. Peplow and K. Verghese. Measured molecular coherent scattering form factors of animal tissues, plastics and human breast tissue. *Phys. Med. Biol.*, 43:2431–52, 1998.

[24] D. E. Raeside. Monte carlo principles and applications. *Phys. Med. Biol.*, 21(2):181–97, 1976.

[25] R. Ribberfors and K. F. Berggren. Incoherent x-ray scattering functions and cross sections $(d\sigma/d\omega')_{incoh}$ by means of a pocket calculator. *Phys. Rev. A*, 26(6):3325–33, 1982.

[26] R. L. Siddon. Fast calculation of the exact radiological path for a three-dimensional CT array. *Med. Phys.*, 12(2):252–5, 1985.

[27] L. Spies, M. Ebert, B. A. Groh, B. M. Hesse, and T. Bortfeld. Correction of scatter in megavoltage cone-beam CT. *Phys. Med. Biol.*, 46:821–33, 2001.

[28] The Scalable Parallel Random Number Generators Library (SPRNG) for ASCI Monte Carlo Computations (SPRNG.) Florida State University. http://sprng.cs.fsu.edu.

[29] M. J. Yaffe and J. A. Rowlands. X-ray detectors for digital radiography. *Phys. Med. Biol.*, 42:1–39, 1997.

[30] H. Zaidi. Comparative evaluation of photon cross-section libraries for materials of interest in pet monte carlo simulations. *IEEE Transactions on Nuclear Science*, 47(6):2722–35, 2000.

[31] W. Zbijewski, A. Colijn, and F. J. Beekman. Monte carlo based scatter correction for cone-beam micro-CT. In *Proc. VIIth Intl. Conf. on Fully 3D Reconstruction and Nuclear Medicine, edited by Y. Bizais*, 2003.

Vita

Noel F. Black received a Ph.D. in theoretical physics in 2002 from the University of Tennessee.